AIAA JOURNAL
Vol. 43, No. 7, July 2005

Transonic Helicopter Noise

A. S. Morgans,* S. A. Karabasov,† A. P. Dowling,‡ and T. P. Hynes§
University of Cambridge, Cambridge, England CB2 1PZ, United Kingdom

Helicopter noise is an increasingly important issue, and at large forward-flight speeds transonic rotor noise is a major contributor. A method for predicting transonic rotor noise, which is more computationally efficient than previous methods and which furthermore offers physical insight into the noise generation, is developed. These benefits combine to make it of potential use to helicopter rotor designers. The permeable surface form of the Ffowcs Williams–Hawkings (FW-H) equation is used to express the sound field in terms of a distribution of monopole and dipole sources over a permeable control surface and a distribution of quadrupole sources over the volume outside of this surface. By choosing the control surface to enclose the transonic flow regions, the noise from the quadrupole distribution becomes negligible. Only the more straightforward surface sources then need be considered, making the acoustic approach computationally efficient. By locating the control surface close to the blade subject to enclosing the transonic flow regions, efficiency in the computational-fluid-dynamics (CFD) approach is also attained. To perform noise predictions, an Euler CFD method to calculate the flowfield was combined with an acoustic method incorporating the retarded time formulation of the FW-H equation. Several rotor blades in hover and steady forward flight were considered, all of which involved transonic flows but for which shock delocalization did not occur. The predictions showed very good agreement with experimental data and with predictions obtained using more computationally intensive methods.

Nomenclature

A	=	$J\lvert\nabla_y f\rvert/\lvert\nabla_\eta f\rvert$
c	=	speed of sound in undisturbed flow, ms^{-1}
f	=	$f=0$ defines location of the control surface S
g	=	$t-\tau-r(\tau)/c$
H	=	Heaviside step function
J	=	Jacobian of $\boldsymbol{y}\rightarrow\eta$ coordinate change
L_i	=	$p_{ij}n_j+\rho u_i(u_n-v_n)$
M	=	magnitude of $\boldsymbol{M}$
$\boldsymbol{M}$	=	Mach-number vector
M_a	=	magnitude of advancing-tip Mach number
M_f	=	magnitude of forward-flight Mach number
M_H	=	magnitude of rotational-tip Mach number
$\boldsymbol{n}$	=	unit vector normal to control surface
p	=	absolute pressure, Pa
p_{ij}	=	compressive stress tensor, Pa
R_{tip}	=	radius of blade tip (= blade span), m
$r(\tau)$	=	$\lvert\boldsymbol{r}(\tau)\rvert$, magnitude of radiation vector, m
$\boldsymbol{r}(\tau)$	=	$\lvert\boldsymbol{x}(t)-\boldsymbol{y}(\tau)\rvert$, radiation vector, m
r_0	=	distance from rotor hub to observer, m
S	=	control surface
T_{ij}	=	Lighthill stress tensor $=\rho u_i u_j+p_{ij}-c^2\rho'\delta_{ij}$
t	=	observer time, s
U_i	=	$(1-\rho/\rho_0)v_i+\rho/\rho_0 u_i$
$\boldsymbol{u}$	=	fluid velocity, ms^{-1}
$\boldsymbol{v}$	=	blade/control surface velocity, ms^{-1}
$\boldsymbol{x}$	=	observer position, m
$\boldsymbol{y}$	=	source position, m
α	=	blade pitch angle, deg
β	=	blade cone angles, deg
δ	=	Dirac delta function
ε	=	rotor disk tilt angle, deg
$\boldsymbol{\eta}$	=	coordinates in which S is stationary
μ	=	helicopter advance ratio, $=M_f/M_H$
ρ	=	density, kgm^{-3}
τ	=	source time, s
$\tau*$	=	retarded time, $=t-r(\tau*)/c$, s
ψ	=	azimuth angle, deg
$\Box^2$	=	wave operator $=(1/c^2)(\partial^2/\partial t^2)-\nabla^2$

Subscripts

n	=	component in surface normal direction
r	=	component in radiation direction
0	=	value in undisturbed fluid

Superscripts

-	=	generalized variable
$'$	=	fluctuation about undisturbed level

Received 25 November 2003; revision received 8 December 2004; accepted for publication 8 December 2004.

*Ph.D. Student, Department of Engineering. Student Member AIAA.
†Postdoctoral Research Associate, Department of Engineering. Member AIAA.
‡Professor of Mechanical Engineering and Head of the Division of Energy, Fluid Mechanics and Turbomachinery, Department of Engineering. Senior Member AIAA.
§Lecturer, Department of Engineering. Member AIAA.

Introduction

In recent years, helicopter noise has become an increasingly important issue. This is due to factors such as environmental acceptability of ground noise levels, passenger comfort, and, for military helicopters, acoustic detectability. At large forward-flight speeds, shock-associated rotor noise is a major noise source. Despite this, there is presently no method of predicting it that is both sufficiently physically insightful and fast to be of full benefit in the rotor design process.

Rotor noise is most efficiently predicted using integral methods that separate the computation of the noise sources and the noise propagation. The aerodynamic field around the blade is evaluated using an unsteady computational fluid dynamics (CFD) solver, and an integral formulation is used to describe how the sound propagates to the far field. The two most commonly used integral methods are the Kirchhoff method and Ffowcs Williams–Hawkings (FW-H) equation.

The Kirchhoff method involves integration over a surface located in the linear flow region.[1–3] It has the advantage of not requiring any volume integration, but its drawback for transonic flows is that the linear flow region is typically far from the blade,[3,4] meaning that

obtaining a CFD solution which remains accurate and well resolved at the surface is computationally intensive. Hence, although the Kirchhoff method has been used to predict transonic rotor noise accurately,[3,5–7] the method is too time consuming for use by designers. Furthermore, it does not provide any physical insight into how the noise is generated.

The FW-H equation expresses the noise in terms of a distribution of monopole and dipole sources over a control surface and a distribution of quadrupole sources over the volume outside the surface.[1] When the control surface is chosen to coincide with the blade surface, these distributions represent the noise due to blade thickness, blade loading and flow non-linearities/entropy variations respectively. It has been shown that the noise generated by the volume quadrupole distribution is negligible for a subsonic volume of fluid but is significant in regions of transonic flow.[8–10] It is generated mainly at the shock surfaces but also near the leading edge of the blade toward the blade tip. Calculating the noise generated by this quadrupole distribution is both time consuming and numerically difficult. Although methods of approximating it exist, there is no satisfactory method of performing the volume integration exactly.

To predict shock-associated noise while avoiding the need to compute the problematic quadrupole term, the FW-H equation can be applied to a permeable control surface that encloses the blade but is not coincident with it. If the control surface is also chosen to enclose all transonic regions of flow, the flow volume outside of the control surface is fully subsonic, and the noise generated by the quadrupole distribution outside of the surface is negligible. Thus by moving the control surface outward, the effect of the quadrupoles within it can be accounted for by the surface source terms. Furthermore, the transonic region is always well defined, and the surface source terms continue to have physical meaning; the monopole distribution is related to mass flux through the surface and the dipole distribution to momentum flux. Also, by comparing the prediction obtained using the permeable control surface to that obtained using the blade surface, the thickness, loading, and shock-associated contributions to the overall noise can be identified.

The permeable surface form of the FW-H equation has recently been used to successfully predict transonic rotor noise.[7,11] However, in these cases the permeable control surfaces were generally larger than necessary to enclose just the transonic flow region, thus resulting in more computational effort than was necessary. To take full advantage of the permeable surface form, the surface should be as small as possible while enclosing all transonic flow regions. This ensures that the quadrupoles responsible for significant noise generation are accounted for, while minimizing the computational effort needed to obtain the surface information.

Acoustic Methodology

Background: The Permeable Surface Form of the FW-H Equation

The permeable surface form of the Ffowcs Williams–Hawkings equation follows from the fluid conservation laws in the same way as the more familiar impermeable surface form.[1]

A permeable control surface S, which is defined by the equation $f(\boldsymbol{x}, t) = 0$, is considered. S encloses all solid boundaries and moves with velocity $\boldsymbol{v}$ (Fig. 1).

Generalized flow variables, which hold over infinite space, are defined (denoted by an overbar). Outside the surface S, the generalized variables are equal to the real flow variables, whereas inside the surface they have the value zero. Where a differential operator acts on a generalized function or variable, it should be assumed that generalized differentiation is implied.[12,13] The continuity and momentum equations valid over all space are

$$H(f)\left[\frac{\partial \rho'}{\partial t} + \frac{\partial (\rho u_i)}{\partial x_i}\right] = 0 \tag{1}$$

$$H(f)\left[\frac{\partial (\rho u_i)}{\partial t} + \frac{\partial}{\partial x_j}(p_{ij} + \rho u_i u_j)\right] = 0 \tag{2}$$

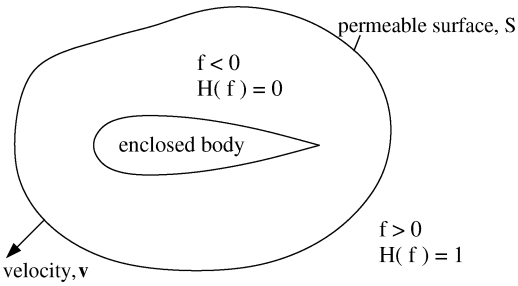

Fig. 1 Permeable control surface.

which can be rearranged to give

$$\frac{\partial \overline{\rho'}}{\partial t} + \frac{\partial (\overline{\rho u_i})}{\partial x_i} = [\rho_0 u_n + \rho'(u_n - v_n)]\delta(f)|\nabla_x f| \tag{3}$$

$$\frac{\partial (\overline{\rho u_i})}{\partial t} + \frac{\partial}{\partial x_j}(\overline{p_{ij}} + \overline{\rho u_i u_j}) = [p_{ij} n_j + \rho u_i (u_n - v_n)]\delta(f)|\nabla_x f| \tag{4}$$

Following the notation of di Francescantonio,[11] new variables U_i and L_i are introduced to simplify the algebra. These represent mass-like and momentum fluxes through S.

$$U_i = (1 - \rho/\rho_0)v_i + \rho/\rho_0 u_i, \qquad L_i = p_{ij} n_j + \rho u_i (u_n - v_n)$$
$$(L_m = L_i M_i) \tag{5}$$

By subtracting the divergence of Eq. (4) from the time derivative of Eq. (3), an inhomogeneous wave equation is obtained:

$$c^2 \Box^2 \rho'(\boldsymbol{x}, t) = -\frac{\partial}{\partial x_i}[L_i \delta(f)|\nabla_x f|] + \frac{\partial}{\partial t}[\rho_0 U_n \delta(f)|\nabla_x f|] + \frac{\partial^2 \overline{T_{ij}}}{\partial x_i \partial x_j} \tag{6}$$

This is the equation governing the generation and propagation of sound and is the differential form of the FW-H equation. On the right-hand side, surface monopole, surface dipole, and volume quadrupole distributions act as acoustic sources, while on the left the wave operator describes the propagation of sound from the sources to the observer. $\overline{T_{ij}}$ is the generalized Lighthill stress tensor, which has value $T_{ij} = \rho u_i u_j + p_{ij} - c^2 \rho' \delta_{ij}$ outside of the surface S. Because S is chosen to enclose the blade and all transonic flow regions, T_{ij} is negligible outside of S, and so the last term on the right can be neglected. This is consistent with the observation that for blades around which the flow is entirely subsonic (up to tip Mach numbers of approximately 0.8) the total noise contribution from T_{ij} is negligible.[14,15]

The equation is valid in all of three-dimensional space, owing to the fact that generalized variables have been used. The integral form can therefore be obtained by convolving with the free space, three-dimensional Green's function for the wave equation, which has the well known form $\delta(t - |\boldsymbol{x}|/c)/(4\pi|\boldsymbol{x}|)$ (Ref. 16). The substitution $p' = c^2 \rho'$ can be made on the left, requiring linearity and no entropy variation at the observer location (although no such restriction is placed on the flow at the control surface).

$$p'(\boldsymbol{x}, t) = -\frac{\partial}{\partial x_i}\int_{-\infty}^{+\infty} \frac{L_i \delta(f)\delta(g)|\nabla_y f|}{4\pi r} d^3\boldsymbol{y}\, \mathrm{d}\tau + \frac{\partial}{\partial t}\int_{-\infty}^{+\infty} \frac{\rho_0 U_n \delta(f)\delta(g)|\nabla_y f|}{4\pi r} d^3\boldsymbol{y}\, \mathrm{d}\tau \tag{7}$$

where $r = |\boldsymbol{x} - \boldsymbol{y}|$ and $g = t - \tau - r/c$.

A coordinate change from fixed coordinates $\boldsymbol{y}$ to coordinates that move with the control surface $\boldsymbol{\eta}$ allows the source strengths to be considered in a frame moving with the surface. The Jacobian for the

coordinate change is J and represents the ratio of volume elements in the $\boldsymbol{\eta}$ and $\boldsymbol{y}$ spaces:

$$p'(\boldsymbol{x},t) = -\frac{\partial}{\partial x_i}\int_{-\infty}^{+\infty}\frac{L_i\delta(f)\delta(g)|\nabla_y f|J}{4\pi r}d^3\boldsymbol{\eta}\,\mathrm{d}\tau + \frac{\partial}{\partial t}\int_{-\infty}^{+\infty}\frac{\rho_0 U_n\delta(f)\delta(g)|\nabla_y f|J}{4\pi r}d^3\boldsymbol{\eta}\,\mathrm{d}\tau \tag{8}$$

Equation (8) is the most general integral form of the permeable FW-H equation. To implement it numerically, it is necessary to integrate the two delta functions. The method of performing these integrations determines which formulation of the FW-H equation is used.

Numerical Implementation of the FW-H Equation

The various possible formulations have previously been discussed in some detail by Brentner.[17] The retarded time formulation is conceptually the most physical and is computationally relatively straightforward to implement. Although it has been demonstrated that it suffers from limitations at tip speeds approaching or exceeding the speed of sound,[18] such conditions are associated with the noisy phenomenon of shock delocalization, and in practice helicopters do not operate in this regime. These high-speed limitations are therefore less important for design applications, and the retarded time formulation is a suitable formulation on which to be basing a realistic transonic noise prediction method.

To obtain the retarded time formulation from Eq. (8), integration over τ is first performed: because the surface S is fixed in $\boldsymbol{\eta}$ coordinates, the $\delta(f)$ term is unaffected by this. Noting that $|\partial g/\partial\tau| = |1 - M_r|$ and integrating over one space dimension using the remaining delta function gives

$$p'(\boldsymbol{x},t) = -\frac{\partial}{\partial x_i}\int_S\left[\frac{L_i A}{4\pi r|1-M_r|}\right]_{\tau*}\mathrm{d}S(\boldsymbol{\eta}) + \frac{\partial}{\partial t}\int_S\left[\frac{\rho_0 U_n A}{4\pi r|1-M_r|}\right]_{\tau*}\mathrm{d}S(\boldsymbol{\eta}) \tag{9}$$

Equation (9) is the permeable surface form of the retarded time formulation with the quadrupole term neglected. $A = J|\nabla_y f|/|\nabla_\eta f|$ represents the ratio of area elements in the $\boldsymbol{\eta}$ and $\boldsymbol{y}$ spaces. If the surface is undistorted in motion, then A is equal to unity. $\tau*$ is the retarded time, given implicitly by the relationship,

$$\tau* = t - r(\tau*)/c = t - [|\boldsymbol{x}(t) - \boldsymbol{y}(\tau*)|]/c \tag{10}$$

Sound emitted by the source at retarded time $\tau*$ will reach the observer at the time of interest t. For a fixed observer position and time and for subsonic surface motion, $\tau*$ can only have one value.

To express Eq. (9) in a form suitable for computation, further manipulation is required. Numerical differentiation of the integrals can be avoided, and the speed and accuracy of the computation are improved if the derivatives are taken inside the integrals.[15] The $\partial/\partial x_i$ can be replaced using Eq. (11) [which can be inferred from Eq. (14) in Ref. 19], and the integration surface $S(\eta)$ is independent of t so that time derivatives inside the integrals can be replaced with $\partial/\partial\tau$ terms using Eq. (12):

$$-\frac{\partial}{\partial x_i}\int_S\left[\frac{Q_i}{r|1-M_r|}\right]_{\tau*}\mathrm{d}S = \frac{\partial}{\partial t}\int_S\left[\frac{Q_i r_i}{cr^2|1-M_r|}\right]_{\tau*}\mathrm{d}S + \int_S\left[\frac{Q_i r_i}{r^3|1-M_r|}\right]_{\tau*}\mathrm{d}S \tag{11}$$

$$\frac{\partial[Q(\tau)]_{\tau*}}{\partial t} = \left[\frac{1}{(1-M_r)}\frac{\partial Q(\tau)}{\partial\tau}\right]_{\tau*} \tag{12}$$

Differentiating and gathering terms together gives the following, where $L_m = L_i M_i$ and $U_{\dot{n}}$ is the component of $\boldsymbol{U}$ in the direction of the rate of change of the surface normal vector in $\boldsymbol{\eta}$ coordinates $\dot{n}$. For a nondeforming control surface, this latter term is zero.

$$4\pi p'(\boldsymbol{x},t) = \int_S\left[\frac{\rho_0(\dot{U}_n + U_{\dot{n}})}{r(1-M_r)^2}\right]_{\tau*}\mathrm{d}S(\boldsymbol{\eta}) + \int_S\left[\frac{\rho_0 U_n[r(\partial\boldsymbol{M}/\partial\tau)_r + c(M_r - |\boldsymbol{M}|^2)]}{r^2(1-M_r)^3}\right]_{\tau*}\mathrm{d}S(\boldsymbol{\eta}) + \frac{1}{c}\int_S\left[\frac{\dot{L}_r}{r(1-M_r)^2}\right]_{\tau*}\mathrm{d}S(\boldsymbol{\eta}) + \int_S\left[\frac{L_r - L_m}{r^2(1-M_r)^2}\right]_{\tau*}\mathrm{d}S(\boldsymbol{\eta}) + \frac{1}{c}\int_S\left[\frac{L_r[r(\partial\boldsymbol{M}/\partial\tau)_r + c(M_r - |\boldsymbol{M}|^2)]}{r^2(1-M_r)^3}\right]_{\tau*}\mathrm{d}S(\boldsymbol{\eta}) \tag{13}$$

Equation (13) is the form of the permeable surface retarded time formulation that has been used for numerical computation. It has been assumed that the control surface motion is subsonic, so that $|1 - M_r| = 1 - M_r$, and that the control surface is undistorted in motion, so that $A = 1$ and $\partial A/\partial\tau = 0$. It is the permeable surface form of what is often referred to as Farassat's formulation 1A (Ref. 15).

In the computer program used to numerically implement the retarded time formulation, it is assumed that the blade is a rigid body which can rotate but not deform. In reality, blade loading can lead to significant blade twist and bending; it is assumed that these can be reasonably well accounted for using modified pitch and cone angles.

Rotation matrices and an overall angular velocity vector are used to describe the effect of the blade pitch, cone, rotation, and rotor disk tilt angles. Positions, velocities, and accelerations in the blade-fixed frame can then be related to values in a stationary frame by combining the matrices/vector with rigid-body relations for rotating reference frames. A knowledge of the helicopter forward-flight behavior is also required.

CFD Methodology

The primary interest is in shock-associated noise, and typically the shock is present over the outer part of the span for azimuthal angles corresponding to the blade advancing. For this phase of the cycle in level flight, the interaction with other blade wakes and the disturbance as a result of the presence of the fuselage and tail rotor are likely to be small. The CFD calculations used to generate the data for the acoustic calculations were therefore performed for a single, oscillating, and advancing blade in an otherwise undisturbed flow.

Calculations were performed using a grid that was fixed relative to the blade, with the problem formulated in terms of the relative velocity as in Zhong and Qin.[20] This made it relatively easy to form smooth acoustic surfaces and to ensure good grid and solution quality in their vicinity. In addition, it removed errors associated with the pitching grid technique,[21] which arise when reinterpolating the solution at each time step onto a new grid position.

Although the blade is treated as a rigid body, this approach has been used successfully to account for a wide range of blade motions, including collective and cyclic pitch variations, tilt, and coning. Noninertial terms caused by the highly convoluted motion of the blade frame appear as volumetric sources in this formulation. It is important to handle these terms in a manner that is compatible with the conservative nature of the discretization scheme for the equations of motion and with the nonreflective nature of the boundary conditions. Provided this is done, however, no extra complication appears to arise from using this accelerating frame approach.[22]

The governing equations were discretized in a control volume fashion by assembling numerical fluxes across interfaces using well-proven shock-capturing methods. The explicit characteristic Roe scheme was implemented together with Van Leer's variable extrapolation (MUSCL) of second/third order in characteristic variables in each grid direction. Unwanted numerical oscillations were minimized using the total-variation-diminishing (TVD) approach, which was applied to limit the slopes of the characteristic variables using the MinMod limiter. Slight modifications were made to the

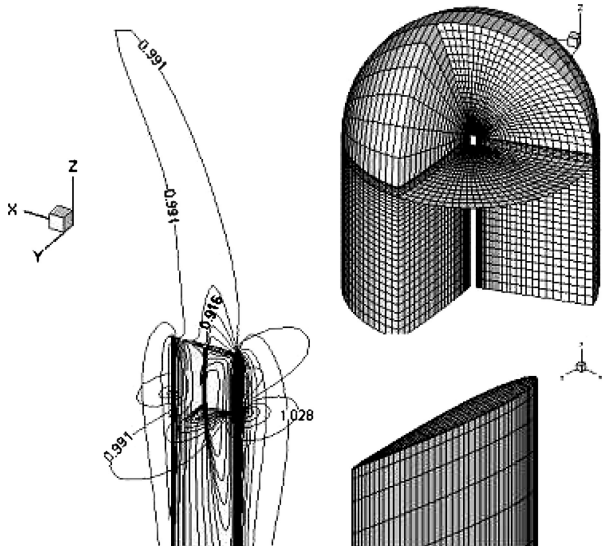

Fig. 2 Computational grid and pressure field around a hovering UH-1H rotor blade at $M_H = 0.88$.

standard MUSCL TVD variable extrapolation formulas to account for nonuniform grid spacing.

The solid-wall rotor-blade boundary conditions were applied by assembling the outer fluxes and eliminating the velocity component normal to the wall. To reduce the entropy generation near the solid boundary, more accurate estimates for fluxes adjacent to the boundary were made by the introduction of symmetric fictitious points lying inside the blade surface. At the outer boundary, a range of nonreflecting boundary conditions were used to judge the domain size necessary to ensure that the solution at the acoustic surfaces was unaffected by the boundary presence.

The computational grid consisted of a series of chordwise O-type grids stacked in the blade spanwise direction. At the blade tip the grid was wrapped around, forming a hemispherical blade cap to provide a uniform mesh distribution away from the blade, as shown in Fig. 2. A modification of the flux assembling procedure was needed for where the confluence of the blade cap radial lines and the blade grid met to ensure that the algorithm remained uniform and conservative. This grid strategy proved to be quite robust in application to a number of blade geometries.

The inviscid solver was tested in a number of one- and two-dimensional initial value problems.[23,24] A simplified but effective way of applying nonreflecting boundary conditions was also developed and tested on a number of problems involving a two-dimensional transonic pitching blade section accelerating and decelerating in the freestream.[25]

The three-dimensional Euler solver has been validated against several hover and forward-flight benchmarks and has been shown to give good agreement of the calculated blade surface/near-field pressure variations with experiments and other calculations. For example, Fig. 3 shows the near-field comparison for a two-blade rotor at $M_H = 0.7634$ and $\mu = 0.25$ at the $r_0/R_{\text{tip}} = 0.88$ blade station in forward flight.[26]

Figure 4 shows the CFD grid used for the more complex rotor-blade geometries of the HELISHAPE test cases, in which the blade is tapered, twisted, and drooped. The calculated blade surface-pressure distributions at two outer blade sections are compared to experimental data for two azimuth angles in Fig. 5. In general the agreement is very good, despite the fact that the numerical model ignores viscous effects, the influence of the other blades, and variations in the blade pitch angle as a result of elasticity.

Noise-Prediction Results

Noise predictions were performed for various rotor blades in three-dimensional motion. In all cases, the flow in the vicinity of the blade was transonic for at least part of the rotational cycle, although

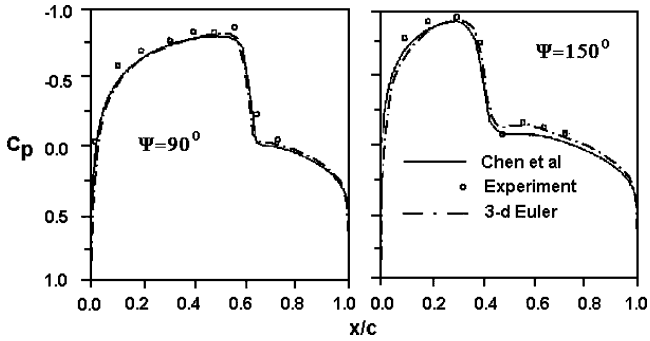

Fig. 3 Simulation of UH-1H-type rectangular unloaded blade in forward flight.

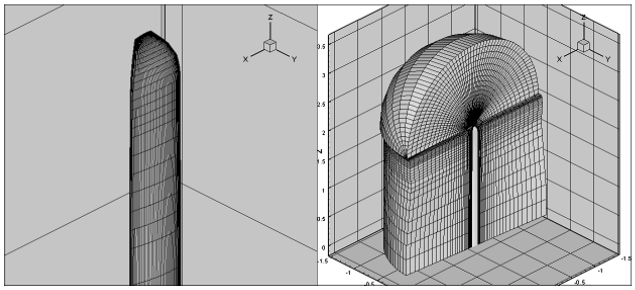

Fig. 4 Blade surface and half-domain CFD grid around the tapered HELISHAPE blade.

tip Mach numbers were sufficiently low to avoid shock delocalization. The CFD method was used to calculate the aerodynamic field around the blade; the permeable surface form of the FW-H equation was then used to generate noise predictions.

Hover

For comparison with available experimental results,[27–30] an isolated UH-1H blade with an aspect ratio of 13.7 was considered in nonlifting hover. Although nonlifting hover does not represent a realistic flight condition, these test cases have become benchmark tests for transonic rotor noise prediction methods and therefore provide a first means of validating the noise prediction approach for three-dimensional motion. They also allow parameters such as CFD grid resolution and control surface location to be investigated.

Because the UH-1H blade is symmetric and nonlifting test cases were being considered, the blade pitch and cone angles were zero. Noise calculations were performed at two different tip Mach numbers, 0.85 and 0.88; for both, a supersonic flow pocket formed on the outer part of the blade and was present throughout the rotational cycle. Previous work[9,27,28] suggested that the tip Mach number marking the onset of shock delocalization for a nonlifting UH-1H blade was between 0.88 and 0.90. The tip Mach numbers of 0.85 and 0.88 should therefore have nondelocalized shocks, although in the $M_H = 0.88$ case the shock will be very close to the onset of delocalization, and hence this is a challenging test case.

Calculations for both tip Mach numbers were performed using two different CFD grid resolutions. The first was a $99 \times 30 \times 36$ grid, meaning that there were 99 grid points in the wraparound direction, 30 in the outward direction, and 36 along the blade span. The second was a finer $139 \times 50 \times 36$ grid. The contours of the Mach number relative to the blade and the pressure as calculated by the CFD solver are shown for both tip Mach numbers and both CFD grids in Figs. 6–9.

For the tip Mach number of 0.85, it can be seen from the Mach-number contours that the supersonic flow region and shock wave are confined to being above/below the blade and do not extend significantly beyond the blade tip. The pressure contours show subtle changes on increasing the grid resolution, but both essentially reveal

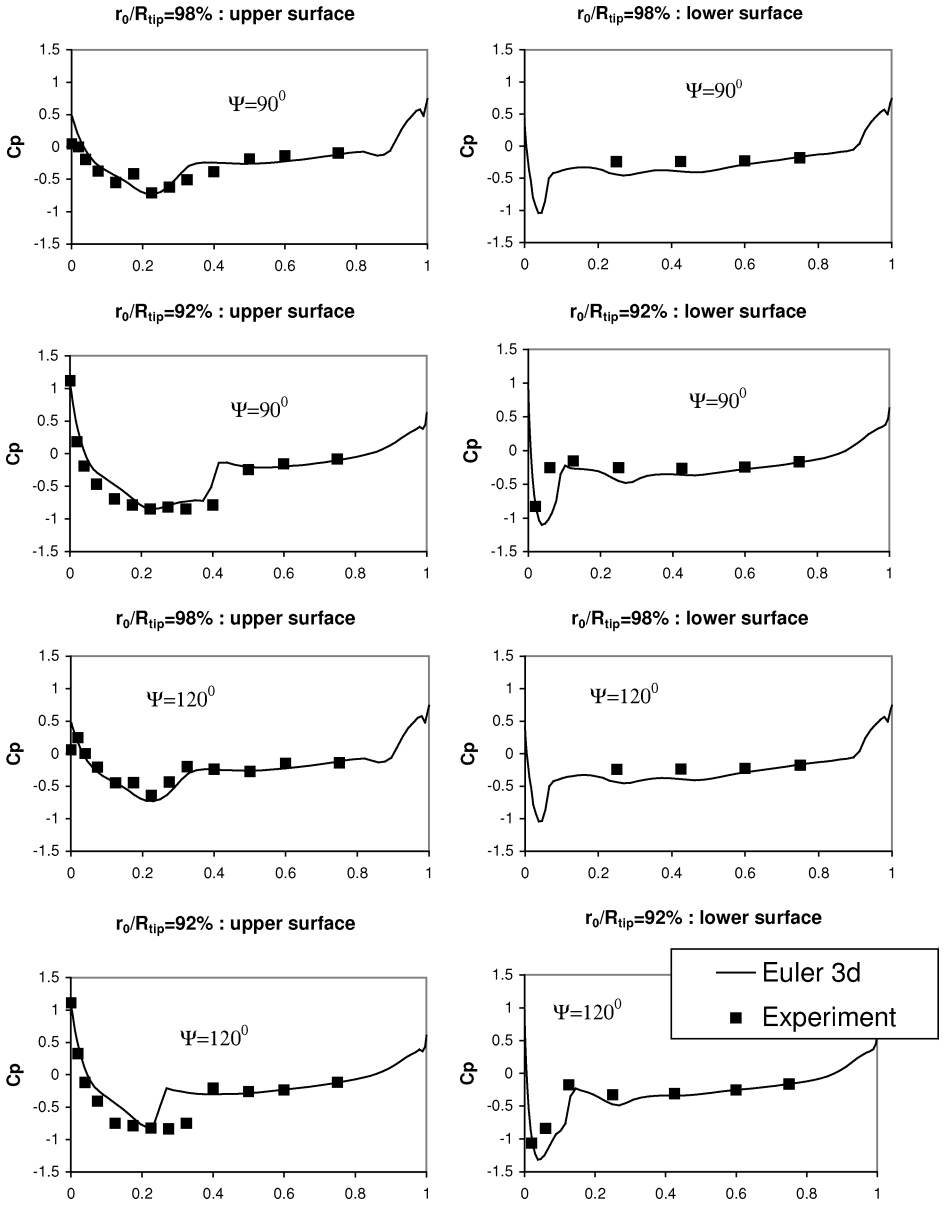

Fig. 5 Computed and experimental pressure coefficients: tapered HELISHAPE blade.

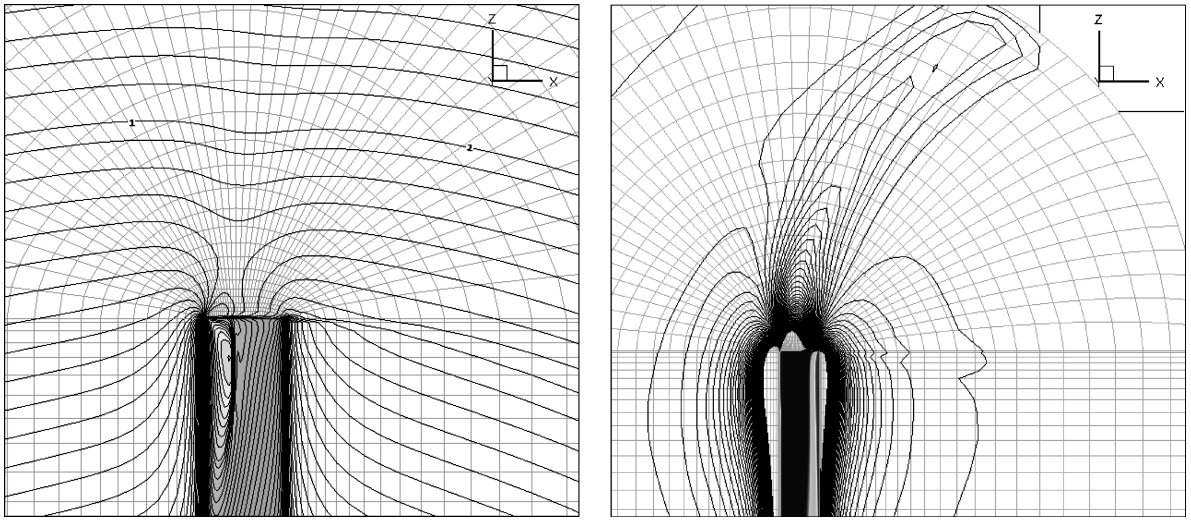

a) **b)**

Fig. 6 Contours of a) relative Mach number and b) pressure for $M_H = 0.85$ and a 99 × 30 × 36 CFD grid.

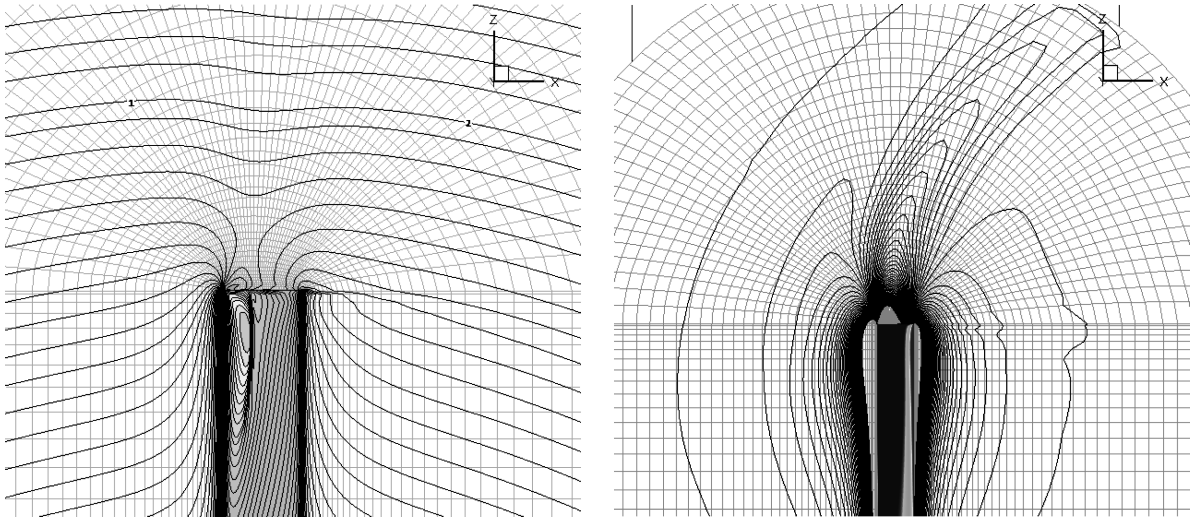

a) b)

Fig. 7 Contours of a) relative Mach number and b) pressure for $M_H = 0.85$ and a 139 × 50 × 36 CFD grid.

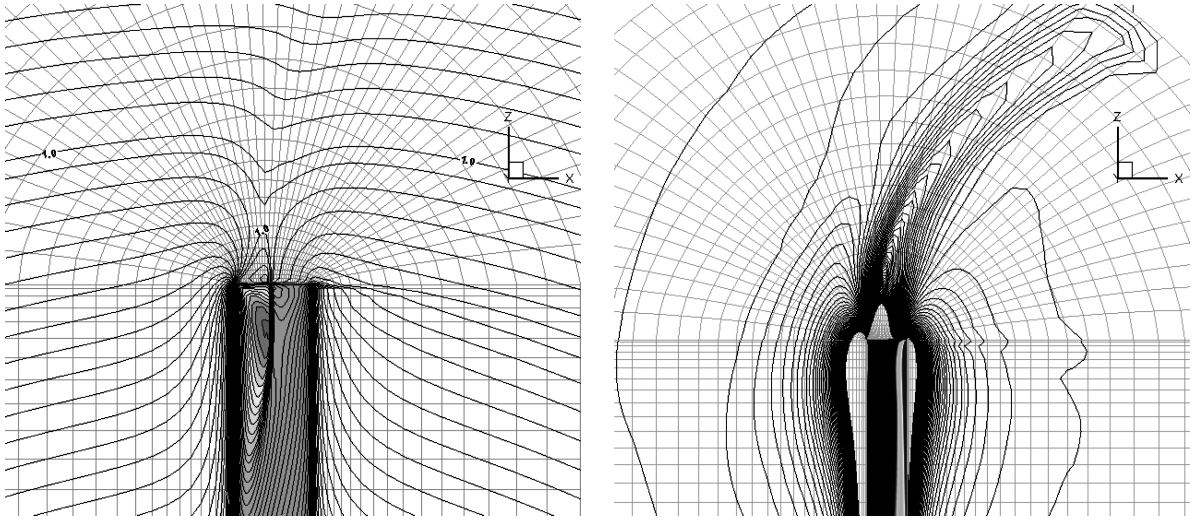

a) b)

Fig. 8 Contours of a) relative Mach number and b) pressure for $M_H = 0.88$ and a 99 × 30 × 36 CFD grid.

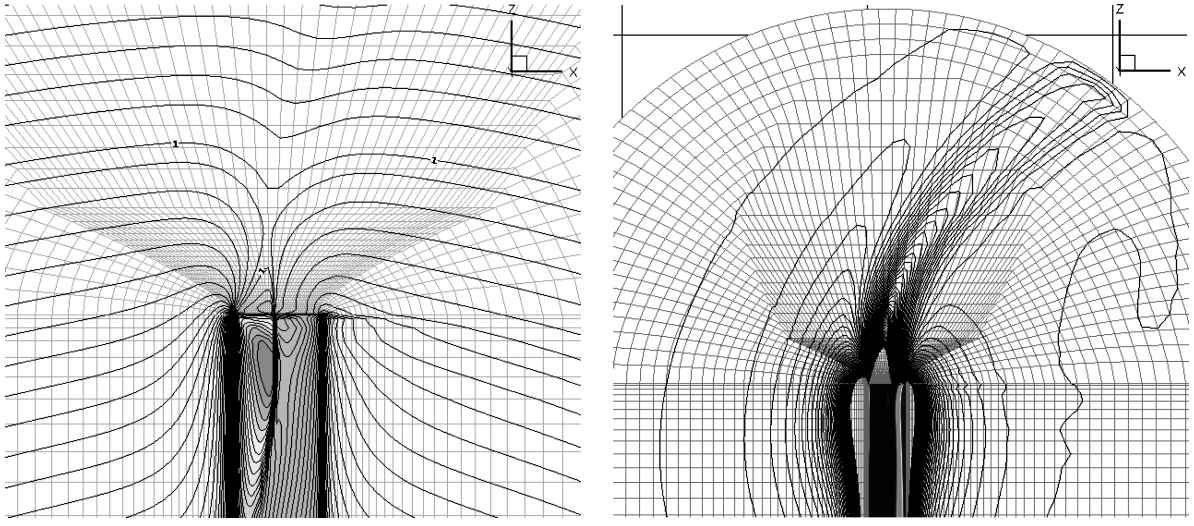

a) b)

Fig. 9 Contours of a) relative Mach number and b) pressure for $M_H = 0.88$ and a 139 × 50 × 36 CFD grid.

the same directionality of the aerodynamic pressure field. For the tip Mach number of 0.88, it can be seen that the supersonic region and hence shock wave do now extend beyond the blade tip. However, they do not intersect the region of the flow, which is supersonic in the frame in which the blade is stationary, meaning that the shock is not delocalized. The pressure contours show minor differences with grid resolution, but both reveal an aerodynamic pressure field with a directionality that is slightly more pronounced than for the tip Mach number of 0.85.

In hover, the inner part of the blade moves at substantially smaller speeds than the outer part. Control surfaces that enclosed only the outer part of the blade and the supersonic flow regions could therefore be used. Examples of the control surfaces used, in this case for the finer grid $M_H = 0.88$ calculations, are shown in Fig. 10. Beyond the blade tip, all pass between the edge of the supersonic region and the radius at which their motion would become sonic. They thus enclose the transonic flow region while undergoing subsonic motion, allowing noise prediction to be carried out via the retarded time formulation of the FW-H equation.

The noise at an observer lying in the rotor plane a distance of 3.09 rotor radii from the axis of rotation was calculated by applying the permeable surface form of the FW-H equation to four different control surfaces for each test case. The innermost control surface extended approximately half a chord beyond the blade leading and trailing edges and approximately 4.5% of the blade span beyond the blade tip, while the outermost extended approximately a chord beyond the blade leading and trailing edges and 9% beyond the blade tip. Because the blade position with respect to the stationary observer was periodic at the blade rotation frequency, the observer sound signature was also periodic. One period of the signature for each of the tip Mach numbers is shown in Figs. 11 and 12.

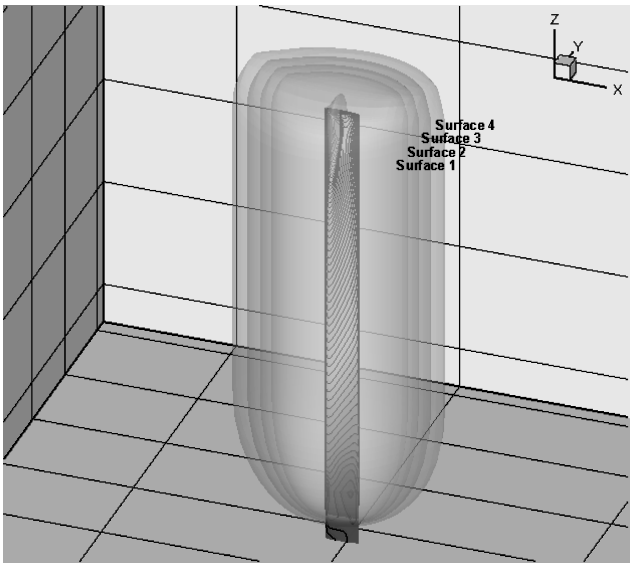

Fig. 10 Four permeable control surfaces and the supersonic flow pocket at $M_H = 0.88$ for the 139 × 50 × 36 CFD grid.

For both rotor tip Mach numbers, the observer pressure signal has the form of a large negative peak preceded and followed by much smaller positive peaks, the characteristic signature of rotor plane shock-associated noise.[3,11,27,28,31] All four control surfaces are seen to predict very similar results. The outermost control surface (surface 4) has the largest maximum speed, and some slight errors as a result of the need for a finer acoustic grid are observed in the predictions for the hover tip Mach number of 0.88.

Experimental noise measurements in the vicinity of the negative pressure peaks exist,[27–30] and by enlarging the scale of the graphs around the negative pressure peak, as in Figs. 13–16, the experimental and predicted results can be compared. The experimental results were for a 1/7th-scale blade model, and so the time axis has been scaled to correspond to a full-size blade. The contributions from the loading and thickness noise are also included, as well as their combined total in the form of a prediction based on the blade surface. The difference between the total noise prediction and the blade surface prediction is the shock-associated noise.

It can be seen that for both tip Mach numbers the predicted and experimental results are in good agreement, although the size of the negative pressure peak is underpredicted by approximately 8% for the tip Mach number of 0.85 and 14% for the tip Mach number of 0.88. In both cases, the largest contribution is from thickness noise, with a smaller but substantial contribution from shock-associated noise. The loading noise contribution is small; the blade is nonlifting, and so all of the loading noise is associated with noncompactness across the blade section and numerical drag. The predicted relative sizes of the thickness, loading, and shock-associated noise contributions are in agreement with previous work.[3,28,31,32]

Because the blade drag is likely to be significantly smaller for the Euler-based predictions than the experiments, the corresponding deficit in loading noise can go some way toward explaining the underprediction of the negative pressure peaks. The larger difference for the tip Mach number of 0.88 might be caused by the extreme sensitivity to tip Mach number that occurs close to the onset of shock delocalization; it was commented in Ref. 28 that the negative pressure peak for the $M_H = 0.89$ case is almost 25% larger than for the $M_H = 0.88$ case. Hence any small inaccuracy in the experimental

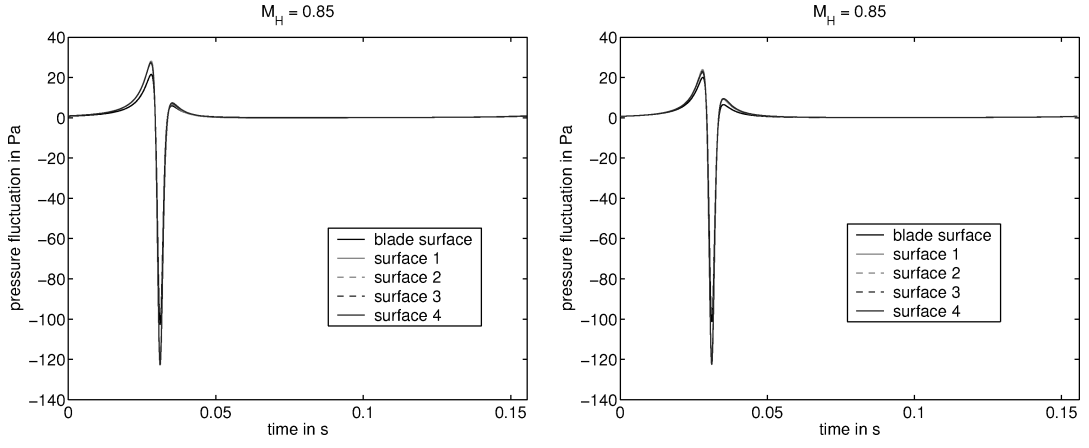

a) b)

Fig. 11 Nonlifting hover at $M_H = 0.85$: one period of the predicted sound for an in-plane observer, $r_0/R_{tip} = 3.09$, a) CFD grids of 99 × 30 × 36 and b) 139 × 50 × 36.

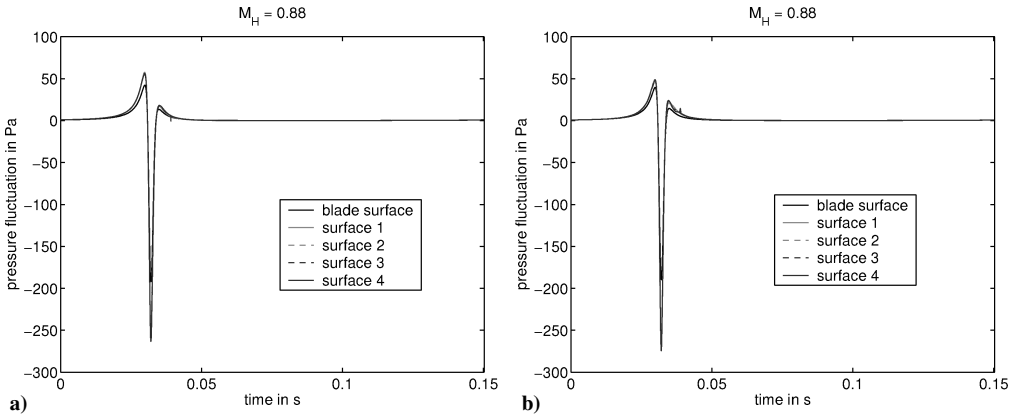

Fig. 12 Nonlifting hover at $M_H = 0.88$: one period of the predicted sound for an in-plane observer, $r_0/R_{tip} = 3.09$, a) CFD grids of 99 × 30 × 36 and b) 139 × 50 × 36.

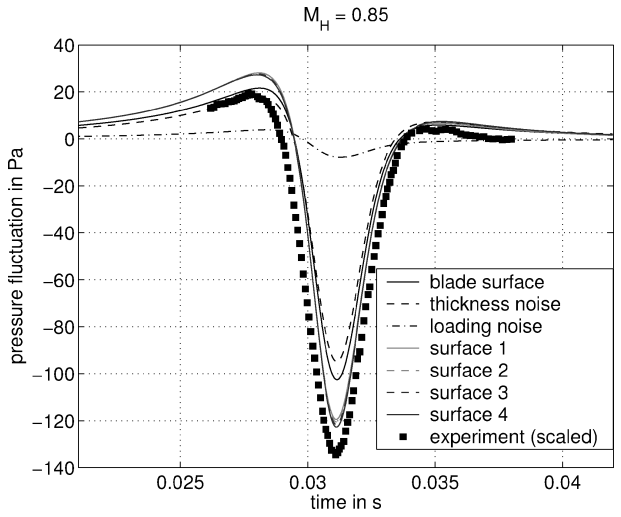

Fig. 13 Nonlifting hover at $M_H = 0.85$: comparison of predictions and experiment, CFD grid of 99 × 30 × 36.

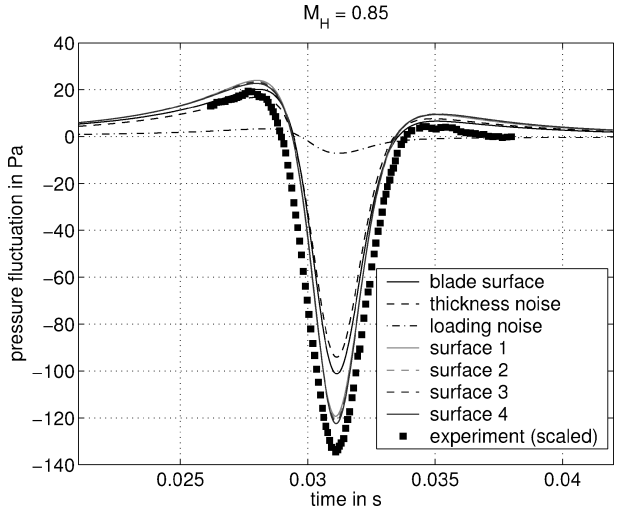

Fig. 14 Nonlifting hover at $M_H = 0.85$: comparison of predictions and experiment, CFD grid of 139 × 50 × 36.

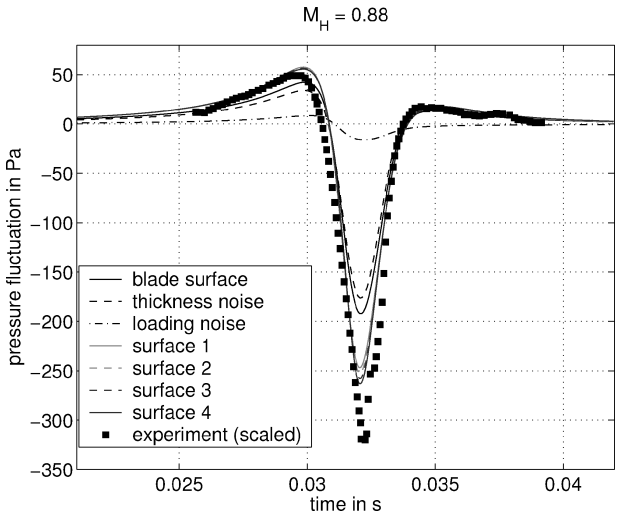

Fig. 15 Nonlifting hover at $M_H = 0.88$: comparison of predictions and experiment, CFD grid of 99 × 30 × 36.

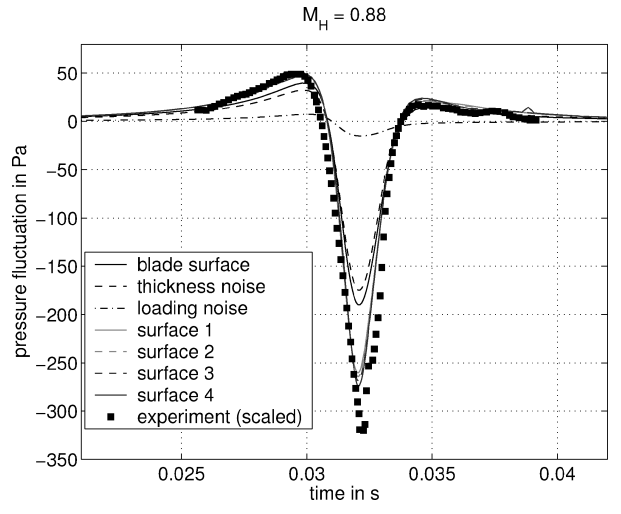

Fig. 16 Nonlifting hover at $M_H = 0.88$: comparison of predictions and experiment, CFD grid of 139 × 50 × 36.

Mach number is likely to result in a much larger percentage deviation in the size of the negative pressure peak. Other transonic noise prediction methods have invariably also underpredicted the size of the 0.88 tip Mach number negative pressure peak, adding weight to this argument.[9,27,28,32,33]

The predictions from the four control surfaces are converged everywhere except in the immediate vicinity of the negative pressure peak for the high-Mach-number case, where small discrepancies exist. For the tip Mach number of 0.85, these discrepancies are almost insignificant, but for the tip Mach number of 0.88 they are larger, showing that the predicted noise is more sensitive to control surface location at this larger tip Mach number.

The predictions obtained using the two different CFD grid resolutions are almost indistinguishable for the tip Mach number of 0.85, suggesting that convergence with grid resolution has been obtained. However, for the tip Mach number of 0.88, the predictions from the

two grids are seen to differ in the region of the negative pressure peak. The finer grid results in the capture of an increased amount of shock-associated noise, which results in the size of the negative pressure peak being approximately 5% larger. The combined contribution of thickness and loading noise is seen to be virtually unaffected, although the loading noise is slightly reduced when using the finer grid, probably because the increased spatial resolution results in reduced numerical drag.

These results confirm that when the flow around the blade is transonic, shock-associated noise contributes significantly to the in-plane negative pressure peak. The contribution increases with blade tip Mach number. Accurate capture of the noise requires use of a sufficiently fine spatial CFD grid and integration over a sufficiently large permeable control surface. The required number of CFD grid points and control surface size both increase with blade tip Mach number.

The results obtained using the permeable surface form of the FW-H equation are compared in Figs. 17 and 18 with recent results obtained using direct Euler CFD calculations,[28] the Kirchhoff method,[3,5] and the impermeable surface form of the FW-H equation with the quadrupole term approximated.[3] The results have been scaled, where necessary, so that they apply to a full-sized UH-1H blade.

The predictions obtained using the permeable surface form of the FW-H equation compare favorably with those from the other prediction methods. Furthermore, because they only require near-field CFD data and surface integration, the approach is the most computationally efficient.

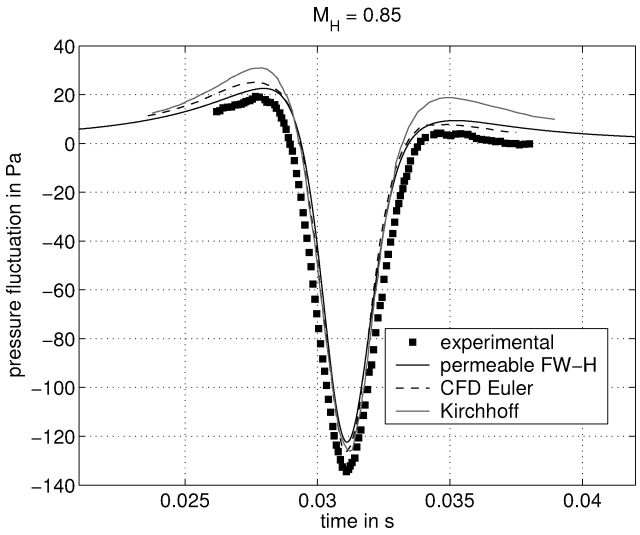

Fig. 17 Comparison of permeable FW-H noise predictions with those from other methods for a nonlifting UH-1H blade in hover: $M_H = 0.85$, and $r_0/R_{\text{tip}} = 3.09$.

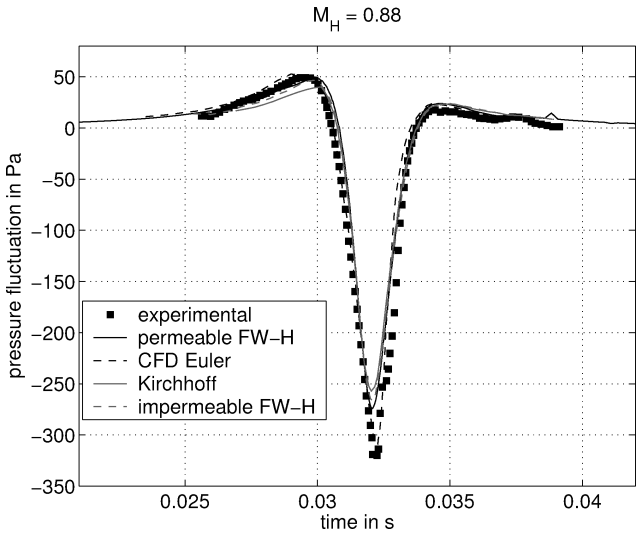

Fig. 18 Comparison of permeable FW-H noise predictions with those from other methods for a nonlifting UH-1H blade in hover: $M_H = 0.88$, and $r_0/R_{\text{tip}} = 3.09$.

Nonlifting Forward Flight

The noise-prediction method is now applied to the more challenging problem of forward flight. For comparison with available experimental results,[27,34,35] a rectangular OLS blade moving at a constant forward-flight speed with a rotational tip Mach number of 0.664, an advance ratio of 0.2605, and an advancing tip Mach number of 0.837 was considered. The blade aspect ratio was 9.22, and the blade was once again nonlifting to avoid vorticity-associated noise. The coning and rotor disk tilt angles were zero.

In forward flight, the blade tip speed varies throughout the rotational cycle. In practice a supersonic flow pocket exists only during the advancing part of the cycle. Using the azimuth convention of ψ increasing in the direction of rotation and being equal to 90 deg at the advancing position and 270 deg at the retreating position, a supersonic flow region existed between azimuth angles of approximately $\psi = 70$ and 135 deg for the test case being considered. The strongest shock occurred at $\psi = 105$ deg, and the Mach contours for this position are shown in Fig. 19. A CFD grid of $139 \times 30 \times 36$ was used.

For a hovering blade, rotating the location of an observer within a horizontal plane while maintaining distance from the blade hub results in a pressure variation that is identical except for a time shift. This is not the case for forward flight; the observer sound signature depends on orientation within the horizontal plane as well as distance from the blade hub. To gain an insight into the rotor plane noise for this forward-flight test case, the sound at three observer locations within the rotor plane was considered. All three observers translated with the same forward-flight speed as the blade hub, such that the distance between the rotation axis and the observers was fixed at $r_0/R_{\text{tip}} = 3.44$. The angle between the observer and the downstream direction was varied as shown in Fig. 20. For the noise predictions, four control surfaces that enclosed the supersonic region when at its largest were used. The innermost surface extended approximately 15% of the blade chord beyond the leading and trailing edges and 2.5% of the span beyond the blade tip, whereas the

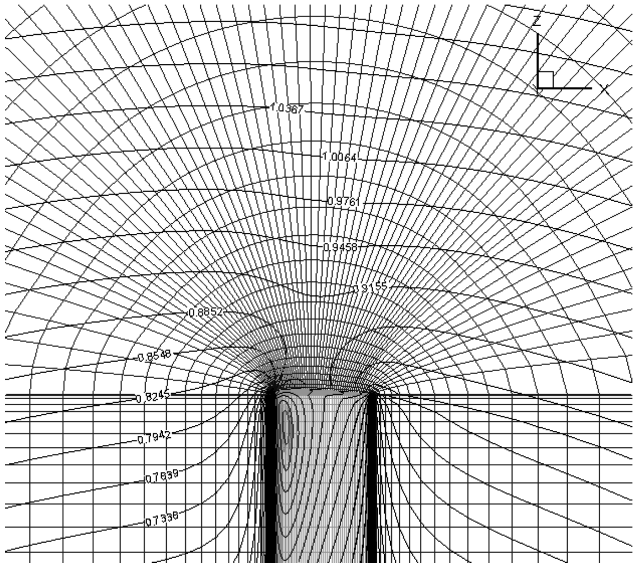

Fig. 19 Contours of Mach-number relative to the blade for the upper blade surface at $\psi = 105$ deg.

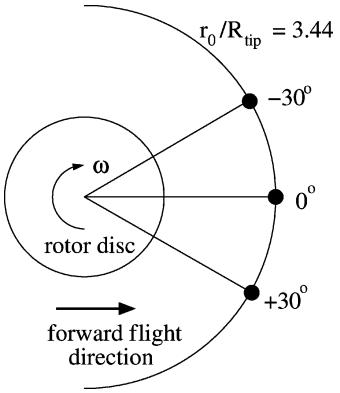

Fig. 20 Observer locations in the frame of the rotation axis.

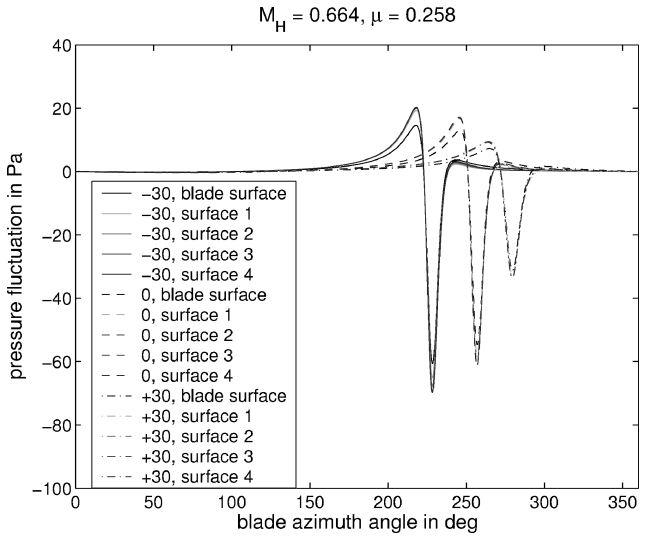

Fig. 21 Forward-flight noise predictions for three rotor plane observers at $r_0/R_{tip} = 3.44$.

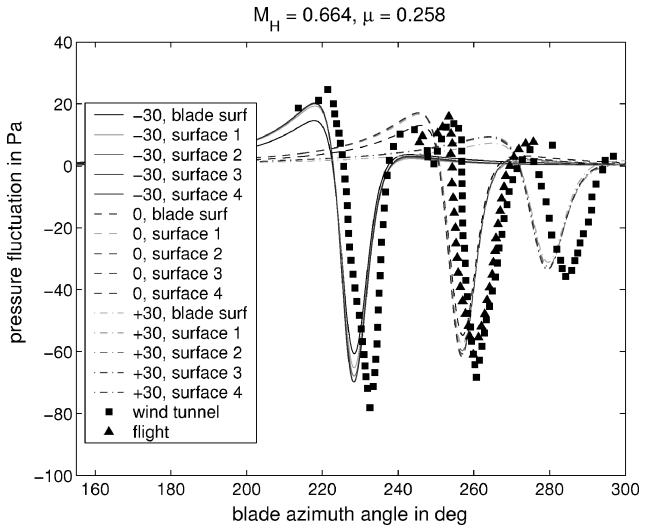

Fig. 22 Comparison of the predicted noise with experimental data.

outermost extended aproximately 85% of the blade chord beyond the leading and trailing edges and 10% of the span beyond the blade tip.

Noise-prediction results for one period of the motion are shown in Fig. 21 and are compared to experimental measurements[27] in Fig. 22. (It is not clear how flight-test results for a nonlifting blade were obtained.) The azimuth angle of the blade when sound is received at the observer $\psi(t)$ is plotted on the x axis. This is equivalent to plotting scaled observer time; it should be noted that $\psi(t)$ is greater than the azimuth angle corresponding to sound emission $\psi(\tau*)$. Noise predictions based on the blade surface are also included; because the blade is nonlifting, these are essentially equal to the contribution from blade thickness noise.

The general shape of the noise prediction is the same for all three observers; a negative pressure peak is immediately preceded and followed by a smaller positive peak. For each of the observers, the predictions from the four control surfaces are in good agreement, with the predictions from the outer two surfaces being almost indistinguishable. This suggests that little extra shock-associated noise could be captured by moving the control surface out further. Once again, thickness noise is the main in-plane component, with a significant additional amount caused by shock-associated noise.

The predicted signatures are in very good agreement with those from experiment, although there is a slight shift in the azimuth response. The reason for this is unclear; although there is some ambiguity in Ref. 27 as to the advance ratio/advancing tip Mach-number combination that has been used, noise predictions have been performed for all possible combinations and confirm that the changes are too subtle to explain the azimuth shift. One possibility is that in-plane bending, known as lead-lag motion, occurs in the experiments and is responsible. The sizes of the negative pressure peaks are underpredicted by approximately 10%, although again this might be partially caused by the loading noise deficit associated with using an Euler CFD code.

For both the predicted and experimental results, the peak response occurs somewhere between the −30- and 0-deg observer stations. This corresponds to a location upstream of the advancing rotor blade. At this location, the Doppler factor $1/|1 - M_r|$ is large, and the radiation vector magnitude r small when the blade speed and shock strength are large; these effects amplify the noise.

Lifting Forward Flight

Noise predictions were now carried out for lifting rotors in forward flight. Two rotors were considered, each composed of four identical blades of radius of 2.1 m and aspect ratio 15. The first rotor was composed of rectangular blades consisting of a spanwise blend of OA213 and OA219 Boeing airfoils; the second was composed of tapered blades with the same spanwise blend of airfoils but with a different geometrical twist, such that the blade tips were slightly swept back and drooped.

For each of the rotors, a different combination of rotational tip Mach number M_H, advance ratio μ, effective rotor disk tilt angle ε_{eff}, and pitch variation $\alpha(t)$ was considered, as summarized in Table 1. The forward flight and advancing tip Mach numbers are denoted by M_f and M_a, respectively. The pitch angle of the blades varied cyclically about the $\frac{1}{4}$-chord axis as a function of blade azimuth angle and was always negative to give upward lift. The blade cone angle was taken to be zero, as indicated in the experimental data, and second-order harmonic flap angles were neglected.

It is clear that the flight parameters for the two cases are very similar, with the advancing tip Mach number differing by less than 0.5%. In both cases, the advancing tip Mach number is sufficiently high so that a shock wave forms above the outer part of the blade during the advancing part of the cycle. The CFD calculations were performed on a $127 \times 30 \times 36$ grid; the pressure contours for the advancing positions are shown in Fig. 23.

For each rotor, the sound at two observers was considered. Both observers translated at the rotor forward-flight speed and were thus fixed with respect to the rotor hub. Such observers are equivalent to stationary microphones within a wind-tunnel, allowing the noise

Table 1 Parameters for the two HELISHAPE test cases

Blade shape	M_H	μ	M_f	M_a	ε_{eff}, deg	α_{av}, deg
Rectangular	0.662	0.331	0.219	0.881	4.81	−7.61
Tapered	0.660	0.328	0.216	0.877	5.10	−7.75

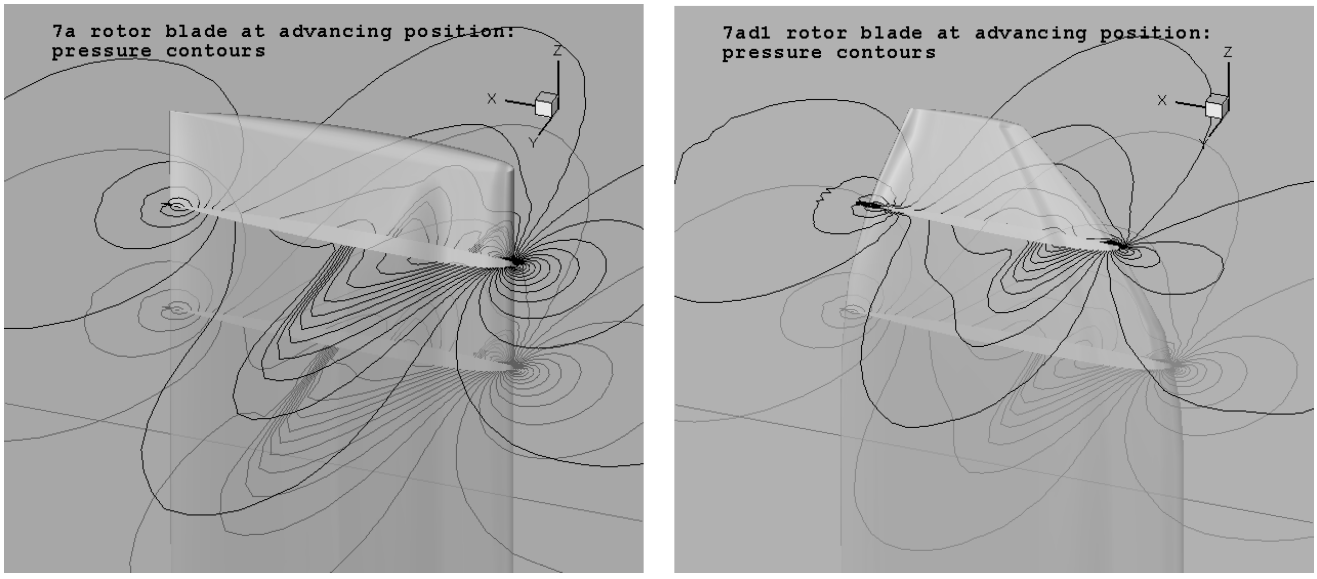

a) b)

Fig. 23 Pressure contours for the advancing position of the a) rectangular and b) tapered blades.

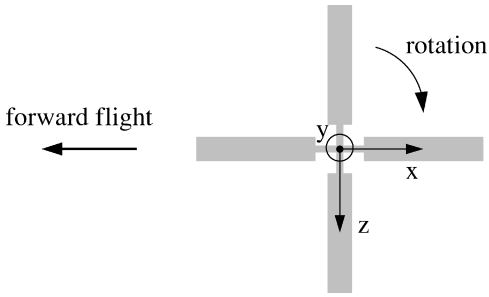

Fig. 24 Coordinate system for forward flight.

predictions and wind-tunnel measurements to be directly compared. It was assumed that the wind-tunnel boundaries were sufficiently far from the rotor for their effect on the measurements to be negligible.

The observer coordinates were (−5.27, −2.28, 2.69) for observer 1 and (−5.27, −2.28, 2.15) for observer 2, where a coordinate system that translates with the rotor hub and uses the convention shown in Fig. 24 was used.

Noise prediction was again carried out using several control surfaces. For the rectangular blades, the innermost control surface extended approximately a chord beyond the leading and trailing edges of the blade and 6.5% of the blade span beyond the blade tip, while the outermost extended approximately two chords beyond the leading and trailing edges and 13% beyond the blade tip. For the tapered blades, the innermost surface extended approximately 0.65 of a chord beyond the leading and trailing edges and 5% of the blade span beyond the blade tip, while the outermost extended approximately two chords beyond the leading and trailing edges and 14% beyond the blade tip.

Because the observers translated at the rotor forward-flight speed, the behavior of each blade relative to the observer was identical except for phase shift or time delay. Noise prediction was therefore carried out for a single rotating blade, and the results were time delayed and summed to obtain the noise prediction for all four blades.

The predictions were compared to measurements from equivalent wind-tunnel test cases. Because the rotor blades were lifting, the comparisons were complicated by the presence of vortex-induced loading noise in the measurements, which could not be accounted for in the predictions as a result of the use of an Euler CFD solver. Some discrepancy between the predicted and measured noise was therefore expected.

The results are shown in Figs. 25 and 26. The observer pressure fluctuations are plotted against nondimensionalized time for one period of the rotor motion. The starting time for the experimental results is arbitrary, and hence a phase difference between the experimental and measured results is expected.

Both the experimental and predicted pressure variations consist of four equally spaced negative pressure peaks, corresponding to the advancing phase of the cycle for each of the four blades. The peaks are separated by regions of positive pressure at low levels, in which a proportionally larger amount of the measured noise is likely to be contaminated by effects such as vortex-induced loading noise.

For both cases, the magnitude of the negative pressure peaks is slightly larger for observer 2 than for observer 1. This is because the z coordinates of the observer positions are 2.69 and 2.15 m, respectively, with the blade radius being 2.1 m. Observer 2 is closer to being directly upstream of the advancing position, meaning that the amplification effects of the Doppler factor and radiation vector are larger.

Despite the fact that the flight condition parameters are very similar for both rotors, the noise levels differ significantly; they are approximately 35% smaller for the rotor with tapered blades. This is primarily because of differences in the shock-associated noise as the thickness and loading contributions are similar. The difference is likely to be associated with the blade shape. Whereas the rectangular blade is unswept, the tapered blade is slightly swept back and drooped at the tip. Sweep serves to reduce the flow Mach number relative to the blade. It therefore follows that the strength of the shock and the shock-associated noise are reduced, an effect that has been observed in the past.[36] The extent of the supersonic region is clearly seen to be smaller for the tapered blade in Fig. 23.

The predicted magnitudes of the negative pressure peaks are approximately 20% less than the measured. However, the predictions from the different control surfaces are converged, suggesting that little extra real quadrupole noise could be captured by further enlarging the control surface. The differences are therefore likely to be caused by physical effects, such as vortex-induced loading noise, which are not accounted for in the noise predictions, the drag deficit associated with the Euler CFD code and CFD grid coarseness.

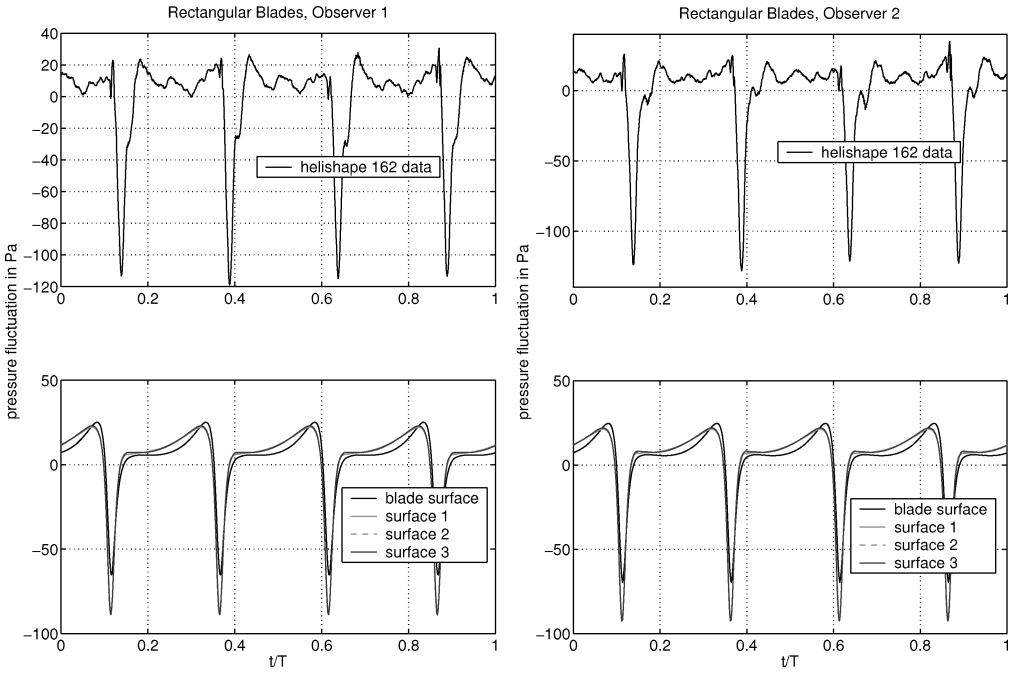

Fig. 25 Observer noise for 1 period of rotor motion, rectangular blades.

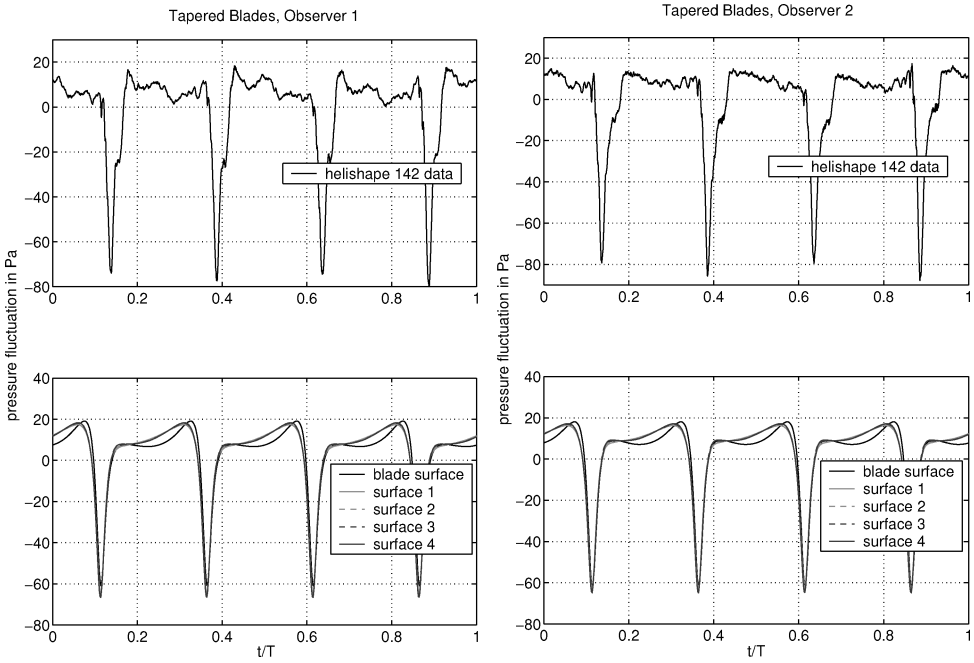

Fig. 26 Observer noise for 1 period of rotor motion, tapered blades.

Conclusions

The permeable form of the Ffowcs Williams–Hawkings (FW-H) equation has been used to predict transonic rotor noise with much less computational effort than has previously been possible. The methodology involved applying the FW-H equation to control surfaces that were very small while enclosing both the blade and all transonic flow regions. Such a choice of control surface ensured that the quadrupole term in the FW-H equation was negligible and meant that an accurate computational-fluid-dynamics (CFD) solution was required only in the vicinity of the blade. This methodology also allowed physical insight into the noise generation to be retained.

Noise predictions for both hover and forward-flight test cases were obtained by using an Euler-based CFD method to calculate the flow variables on the control surface. The permeable surface form of the FW-H equation (the retarded time formulation with the quadrupole term neglected) was then used to calculate the propagation of sound from the control surface to the observer. The noise predictions showed very good agreement with experimental results, validating the methodology.

Acknowledgments

The authors are grateful to the Engineering and Physical Sciences Research Council, Westland Helicopters, Ltd., and Thales Underwater Systems, Ltd., for their financial support. They also thank Westland Helicopters, Ltd., for providing the HELISHAPE measurements and V. Kloeppel of Eurocopter Deutschland for providing permission to publish them.

References

[1]Ffowcs Williams, J. E., and Hawkings, D. L., "Sound Generation by Turbulence and Surfaces in Arbitrary Motion," *Philosophical Transactions of the Royal Society*, Vol. A264, May 1969, pp. 321–342.

[2]Lyrintzis, A. S., "Review: The Use of Kirchhoff's Method in Computational Aeroacoustics," *Journal of Fluids Engineering*, Vol. 116, Dec. 1994, pp. 665–676.

[3]Brentner, K. S., Lyrintzis, A. S., and Koutsavdis, E. K., "Comparison of Computational Aeroacoustic Prediction Methods for Transonic Rotor Noise," *Journal of Aircraft*, Vol. 34, No. 4, 1997, pp. 531–538.

[4]Meadows, K. R., and Atkins, H. L., "Towards a Highly Accurate Implementation of the Kirchhoff Approach for Computational Aeroacoustics," *Journal of Computational Acoustics*, Vol. 4, No. 2, 1996, pp. 225–241.

[5]Lyrintzis, A., and Xue, Y., "Versatile Kirchhoff Code for Aeroacoustic Predictions," *AIAA Journal*, Vol. 35, No. 1, 1997, pp. 198–200.

[6]Farassat, F., and Myers, M. K., "Extension of Kirchhoff's Formula to Radiation from Moving Surfaces," *Journal of Sound and Vibration*, Vol. 123, No. 3, 1988, pp. 451–460.

[7]Brentner, K. S., and Farassat, F., "Analytical Comparison of the Acoustic Analogy and Kirchhoff Formulation for Moving Surfaces," *AIAA Journal*, Vol. 36, No. 8, 1998, pp. 1379–1386.

[8]Hanson, D. B., and Fink, M. R., "The Importance of Quadrupole Sources in Prediction of Transonic Tip Speed Propeller Noise," *Journal of Sound and Vibration*, Vol. 62, No. 1, 1979, pp. 19–38.

[9]Schmitz, F. H., and Yu, Y. H., "Helicopter Impulsive Noise: Theoretical and Experimental Status," *Journal of Sound and Vibration*, Vol. 109, No. 3, 1986, pp. 361–427.

[10]Farassat, F., and Tadghighi, H., "Can Shock Waves on Helicopter Rotors Generate Noise? A Study of the Quadrupole Source," *Annual Forum Proceedings, American Helicopter Society*, Vol. 1, American Helicopter Society, Alexandria, VA, 1990, pp. 323–346.

[11]di Francescantonio, P., "A New Boundary Integral Formulation for the Prediction of Sound Radiation," *Journal of Sound and Vibration*, Vol. 202, No. 4, 1997, pp. 491–509.

[12]Gel'fand, I. M., and Shilov, G. E., *Generalized Functions Volume 1: Properties and Operations*, Academic Press, London, 1964.

[13]Farassat, F., "Introduction to Generalized Functions with Applications in Aerodynamics and Aeroacoustics," NASA TP-3428, 1994.

[14]Brentner, K. S., "Prediction of Helicopter Rotor Discrete Frequency Noise—A Computer Program Incorporating Realistic Blade Motions and Advanced Acoustic Formulation," NASA TM 87721, 1986.

[15]Farassat, F., and Succi, G. P., "The Prediction of Helicopter Rotor Discrete Frequency Noise," *Vertica*, Vol. 7, No. 4, 1983, pp. 309–320.

[16]Crighton, D. G., Dowling, A. P., Ffowcs Williams, J. E., Heckl, M., and Leppington, F. G., *Modern Methods in Analytical Acoustic*s, Springer-Verlag, London, 1992.

[17]Brentner, K. S., "Numerical Algorithms for Acoustic Integrals with Examples for Rotor Noise Prediction," *AIAA Journal*, Vol. 35, No. 4, 1997, pp. 625–630.

[18]Morgans, A. S., and Dowling, A. P., "The Aeroacoustics of Transonic Helicopter Blades," AIAA Paper 2002-2545, June 2002.

[19]Farassat, F., "Linear Acoustic Formulas for Calculation of Rotating Blade Noise," *AIAA Journal*, Vol. 19, No. 9, 1981, pp. 1122–1130.

[20]Zhong, B., and Qin, N., "Non-Inertial Multiblock Navier–Stokes Calculation for Hovering Rotor Flow Fields Using Relative Velocity Approach," *Aeronautical Journal*, Vol. 105, No. 1049, 2001, pp. 379–389.

[21]Shaw, S. T., and Qin, N., "Unsteady Flow Around Helicopter Blade Sections in Forward Flight," *Aeronautical Journal of the Royal Aeronatical Society*, Vol. 103, No. 1019, 1999, pp. 35–44.

[22]Karabasov, S. A., and Hynes, T. P., "A Method for Solving Compressible Flow Equations in an Unsteady Free Stream," *Journal of Mechanical Engineering Science* (submitted for publication).

[23]Goloviznin, V. M., Hynes, T. P., and Karabasov, S. A., "CABARET Finite-Difference Schemes for the One-Dimensional Euler Equations," *Mathematical Modelling and Analysis*, Vol. 6, No. 2, 2001, pp. 210–220.

[24]Karabasov, S. A., and Hynes, T. P., "Unsteady Calculation of 2-D Inviscid Flow with Shocks," 6th International Conf. MMA, 2001.

[25]Karabasov, S. A., and Hynes, T. P., "Open Boundary Conditions of Predictor-Corrector Type for External Flows," AIAA Paper 2002-2442, June 2002.

[26]Chen, C. L., McCroskey, W. J., and Obayashi, S., "Numerical Solutions of Forward-Flight Rotor Flow Using an Upwind Method," *Journal of Aircraft*, Vol. 28, No. 6, 1991, pp. 374–380.

[27]Baeder, J. D., "Euler Solutions to Nonlinear Acoustics of Non-Lifting Rotor Blades," International Technical Specialists Meeting on Rotorcraft Acoustics and Rotor Fluid Dynamics, Oct. 1991.

[28]Baeder, J. D., Gallman, J. M., and Yu, Y. H., "A Computational Study of the Aeroacoustics of Rotor in Hover," *Journal of the American Helicopter Society*, Vol. 42, No. 1, 1997, pp. 39–53.

[29]Purcell, T. W., "CFD and Transonic Helicopter Sound," 14th European Rotorcraft Forum, No. 2, 1988.

[30]Boxwell, D. A., Yu, Y. H., and Schmitz, F. H., "Hovering Impulsive Noise: Some Measured and Calculated Results," *Vertica*, Vol. 3, No. 1, 1979, pp. 35–45.

[31]Tadghighi, H., Holz, R., Farassat, F., and Lee, Y. J., "Development of a Shock Noise Prediction Code for High Speed Helicopters—The Subsonically Moving Shock," American Helicopter Society, May 1991.

[32]Brentner, K. S., and Farassat, F., "Modeling Aerodynamically Generated Sound of Helicopter Rotors," *Progress in Aerospace Sciences*, Vol. 39, No. 2–3, 2003, pp. 83–120.

[33]Wang, G., Sankar, L. N., and Tadghighi, H., "Prediction of Rotorcraft Noise with a Low-Dispersion Finite Volume Scheme," *AIAA Journal*, Vol. 38, No. 3, 2000, pp. 395–401.

[34]Schmitz, F. H., and Boxwell, D. A., "In-Flight Far-Field Measurement of Helicopter Impulsive Noise," *Journal of the American Helicopter Society*, Vol. 21, No. 4, 1976, pp. 2–16.

[35]Boxwell, D. A., Schmitz, F. H., Splettstoesser, W. R., and Schultz, K. J., "Model Helicopter Rotor High Speed Impulsive Noise-Measured Acoustics and Blade Pressures," 9th European Rotorcraft Forum, No. 17, 1983.

[36]Pike, A. C., and Harrison, R. J., "Helicopter Noise Measurements at High Advancing Blade Mach Number—A Novel Approach to Full Scale Flight Testing," American Helicopter Society, Oct. 1995.

H. Atassi
Associate Editor